Engineering 48 (2025) 81–91

Contents lists available at ScienceDirect

Engineering

journal homepage: www.elsevier.com/locate/eng

Research
Carbon Capture, Utilization, and Storage—Article

Multiphase Reactive Flow During CO_2 Storage in Sandstone

Rukuan Chai [a,*], Qianqian Ma [a], Sepideh Goodarzi [a], Foo Yoong Yow [b], Branko Bijeljic [a], Martin J. Blunt [a]

[a] Department of Earth Science and Engineering, Imperial College London, London SW7 2AZ, UK
[b] Petroliam Nasional Berhad (PETRONAS), Selangor 43000, Malaysia

ARTICLE INFO

Article history:
Received 26 November 2024
Revised 1 January 2025
Accepted 21 January 2025
Available online 24 February 2025

Keywords:
Geological CO_2 storage
Multiphase reactive flow
Geochemical reactions
Relative permeability

ABSTRACT

Geological CO_2 storage is a promising strategy for reducing greenhouse gas emissions; however, its underlying multiphase reactive flow mechanisms remain poorly understood. We conducted steady-state imbibition relative permeability experiments on sandstone from a proposed storage site, complemented by *in situ* X-ray imaging and *ex situ* analyses using scanning electron microscopy (SEM) and energy-dispersive X-ray spectroscopy (EDS). Despite our use of a brine that was pre-equilibrated with CO_2, there was a significant reduction in both CO_2 relative permeability and absolute permeability during multiphase flow due to chemical reactions. This reduction was driven by decreased pore and throat sizes, diminished connectivity, and increased irregularity of pore and throat shapes, as revealed by *in situ* pore-scale imaging. Mineral dissolution, primarily of feldspar, albite, and calcite, along with precipitation resulting from feldspar-to-kaolinite transformation and fines migration, were identified as contributing factors through SEM–EDS analysis. This work provides a benchmark for storage in mineralogically complex sandstones, for which the impact of chemical reactions on multiphase flow properties has been measured.

1. Introduction

Anthropogenic carbon dioxide (CO_2) emissions, which account for over 75% of global greenhouse gases, are the primary driver of accelerating climate change [1]. The Intergovernmental Panel on Climate Change warns that, without urgent action to reduce emissions—specifically a 43% reduction from 2019 levels by 2030—global temperatures could exceed 1.5 °C as early as 2030 [2]. Geological CO_2 storage is a critical component of climate mitigation strategies [3,4], with the capacity to permanently sequester billions of tons of CO_2 and facilitate deep decarbonization. Sandstone formations are frequently targeted for CO_2 storage due to their widespread availability, structural stability, high porosity, and ability to securely trap CO_2. However, during CO_2 injection, the formation of acidic CO_2–saturated brine inevitably triggers reactions with the minerals in the sandstone [5]. Robust findings from experiments and simulations by Cui et al. [6], Luhmann et al. [7], and Ma et al. [8] demonstrate that these geochemical reactions can have a significant impact on key performance metrics, including the CO_2 injectivity, storage capacity, and long-term safety of the storage site.

Extensive research has been carried out on reactive flow during CO_2 injection into sandstone, with a principal focus on the effect of reactive flow on absolute permeability [9]. However, the conclusions vary considerably, depending on the exact composition of the rock considered. A common finding is a reduction in permeability, which has been attributed to mechanisms such as the precipitation of secondary minerals [7,8,10,11], the dislodging and blockage of clay and quartz particles [12–14], mechanical weakening and compaction [5], and hydrodynamic effects [15]. Dávila et al. [16] reported decreases in both porosity and permeability, with simulations suggesting the precipitation of montmorillonite and mesolite, alongside the dissolution of K-feldspar, calcite, and illite. In contrast, Lamy-Chappuis et al. [17], Zou et al. [18], Tang et al. [19], Sun et al. [20], and Gholami and Raza [21] reported increased permeability following CO_2 injection, attributing it to the dissolution of carbonate cement, alkali feldspar, and clay minerals. Sayegh et al. [22] noted an initial permeability reduction due to fines migration blocking the pore throats, followed by an increase in permeability as these fines were later dissolved. Al-Yaseri et al. [23] suggested that permeability is influenced by both

* Corresponding author.
E-mail address: r.chai@imperial.ac.uk (R. Chai).

https://doi.org/10.1016/j.eng.2025.01.016

sandstone mineralogy and brine composition, with permeability increasing during low-salinity CO_2-saturated water injection but decreasing under high-salinity conditions.

Less work has explicitly studied the effect of reactions on multiphase flow properties. Ge et al. [24] proposed that CO_2-saturated water injection induces fines migration and mineral reactions, resulting in a reduction in CO_2 drainage relative permeability, while the relative permeability of the water remains unaffected. In a related study, Gholami and Raza [21] observed that calcite precipitation, clay dissolution, and a reduction in quartz hydrophilicity collectively increased porosity and absolute permeability but decreased CO_2 relative permeability. Similarly, Kou et al. [25] found that carbonate mineral dissolution dominated over precipitation, leading to increased porosity and permeability, enhanced CO_2 wettability, reduced brine relative permeability, and increased CO_2 relative permeability. Sun et al. [20] suggested that the reaction between carbonic acid and tight sandstone during CO_2 injection increased porosity and permeability, reduced CO_2 relative permeability, and initially decreased brine relative permeability at low CO_2 saturation, which then increased as CO_2 saturation rises. These studies highlight the variability and inconclusiveness of laboratory results, underscoring the need for further investigation into the precise characteristics of reactive flow and its underlying mechanisms. In particular, the effect of mineralogical changes on relative permeability in a reservoir sandstone—representative of a putative storage formation—has not been investigated and is thus the focus of this study.

The exact reactions among CO_2, brine, and sandstone have been extensively studied in autoclaves and batch reactors. Liu et al. [26] injected CO_2 into sandstone/hot water systems and observed sandstone dissolution, along with the deposition of aluminum silicate and calcium–aluminosilicate secondary minerals. Kaszuba et al. [27] and Ilgen et al. [28] found magnesite precipitation and noted the dissolution of silicate minerals and calcite/dolomite, respectively, in CO_2 treatment. Fu et al. [29] and Lu et al. [30] reported extensive feldspar dissolution and secondary mineral precipitation involving iron minerals and kaolinite on feldspar surfaces after CO_2 exposure. Furthermore, Dawson et al. [31] and Pearce et al. [32,33] found that, while carbonate cements dissolved, low-surface-area K-feldspar grains remained unreactive in Berea sandstone exposed to CO_2 in sodium chloride (NaCl) brine. They also observed the dissolution and precipitation of carbonate and silicate minerals, along with the precipitation of barite, iron (Fe)-oxides, clays, and gypsum, as well as ion leaching from Fe-rich chlorite, clay structural collapse, and fines migration during impure CO_2 injection into clay-rich mudstone cores. Carroll et al. [34] proposed that clay dissolution and secondary mineral precipitation, including amorphous silica and kaolinite, were dominant during CO_2–mineral reactions. Fuchs et al. [35] aged sandstone in CO_2–saturated brine for four or eight weeks and revealed the loss of clay cementation, greater exposure of quartz and K-feldspar grains, and apparent surface roughening. While these studies offer valuable insights into the mineral reactions occurring during CO_2 injection, they fail to quantitatively correlate these reactions with the resulting alterations in petrophysical properties, and they do not sufficiently capture the complexities of multiphase reactive flow in sandstone formations.

In light of these findings, we investigate the characteristics and mechanisms of multiphase reactive flow during CO_2 storage in sandstone through steady-state relative permeability experiments, *in situ* imaging, and *ex situ* scanning electron microscopy (SEM) and energy-dispersive X-ray spectroscopy (EDS) analyses. Our objectives are threefold: ① to characterize multiphase reactive flow behavior, ② to identify alterations in pore structure, and ③ to unravel the underlying CO_2–brine–rock reactions during CO_2 injection into sandstone.

2. Materials and methods

2.1. Rock samples and fluid properties

We used a cylindrical sandstone sample sourced from a depleted gas reservoir, with a diameter of (6.03 ± 0.05) mm and a length of (20.05 ± 0.05) mm. The sample exhibited a helium porosity of 25.0%, and its absolute permeability was measured to be (185 ± 10) mD; 1 mD = 0.987×10^{-11} cm^2.

The brine used in this experiment was deionized water doped with 30 wt% potassium iodide (KI). This concentration was selected to facilitate phase segmentation in image analysis, following the methodology of Lin et al. [36]. At the experimental conditions of 50 °C and 8 MPa, the viscosities of the CO_2 and brine were (0.020 ± 0.001) [37] and (0.60 ± 0.05) mPa·s [38], respectively, with an interfacial tension of approximately 35 $mN \cdot m^{-1}$ [39].

2.2. Experimental methods

2.2.1. Steady-state relative permeability experiment

The sample was dried for 24 h in a vacuum oven, enclosed in a Viton sleeve capped with end fittings connected to tubing, and assembled within an aluminum core holder. The core holder was placed inside a micro-computed tomography (micro-CT) scanner (Zeiss Xradia Versa 510), with tubing connections established to the brine and CO_2 supplies, the receiving and confining pumps, and the reactor and pressure transducer. A water bath circulator was used to maintain the temperature in the pumps, while a heating jacket, controlled by a proportional–integral–derivative (PID) system [40,41], regulated the temperature of the core holder, as shown in Fig. 1. To minimize mass transfer between the CO_2 and brine during the experiment, the brine was pre-saturated with CO_2, and the CO_2 was pre-saturated with brine inside the reactor.

A confining pressure of 2.0 MPa was applied, and the sample was initially scanned at a voxel size of 6.5 μm for saturation analysis. Subsequently, a higher-resolution scan (voxel size: 2.9 μm) was performed to assess pore structure, contact angle, and curvature. CO_2 was injected for 30 min to dislodge any fine particles within the sample, followed by a 12 h system vacuuming. Brine was then injected at flow rates of 0.20, 0.50, and 1.00 $mL \cdot min^{-1}$, while the pressure differential was monitored to determine the absolute permeability using Darcy's law. Afterward, the injection rate was reduced to 0.20 $mL \cdot min^{-1}$, and scanning was conducted to capture a fully brine-saturated image. Relative permeability was measured using the steady-state method across a series of brine fractional flows (the volume fraction of brine injected, f_w = 0, 0.05, 0.10, 0.30, 0.70, 0.90, and 1.00), maintaining a constant total flow rate of 0.20 $mL \cdot min^{-1}$. The data at f_w = 1.00 was obtained from another core drilled adjacently, with similar porosity and permeability, and subjected to the same experimental procedure. Each fractional flow required approximately 24 h to reach a steady state, after which the sample was scanned using the same imaging protocol. The experimental procedures were consistent with those reported by Krevor et al. [42] and Gao et al. [43].

After completing all the fractional flow experiments, the sample was extracted, and the pressure drop along the tubing was measured. These pressure drops were subtracted from the measured pressure differences to calculate the absolute and relative permeability. The extracted sample was then dried in a vacuum oven for 24 h, after which a dry scan was conducted to assess changes in pore structure and mineralogy. Finally, the sample's absolute permeability was measured as previously described.

For imaging, we used a Zeiss XRM-510 micro-CT scanner with an X-ray energy of 80.0 keV and a power setting of 7.0 W. Each scan comprised 3201 projections, with an exposure time of 2 s

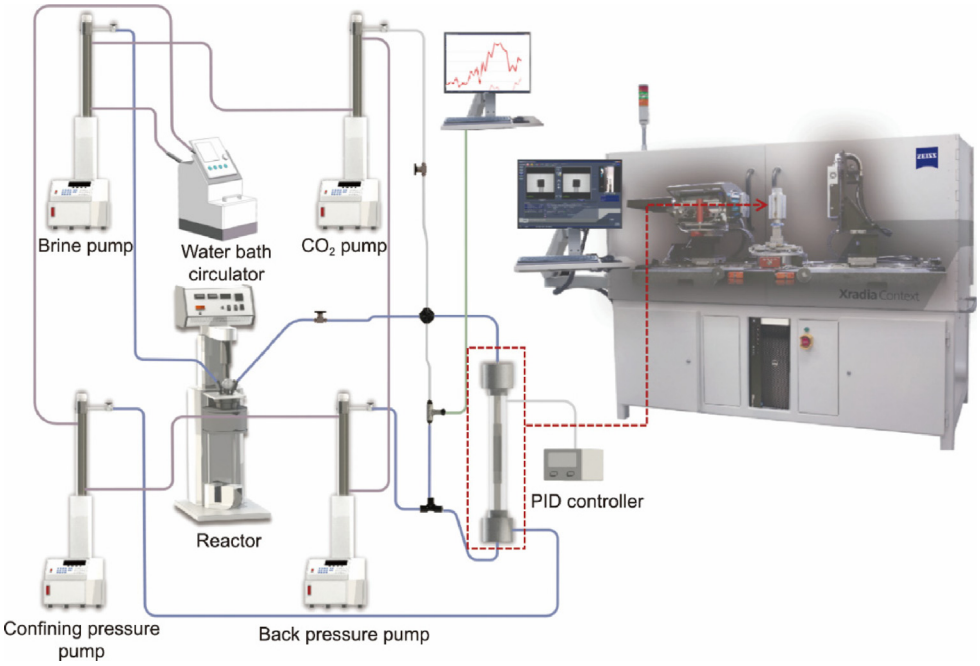

Fig. 1. Schematic diagram of the experimental apparatus.

and a binning factor of 2. Image reconstruction was carried out using Zeiss Reconstructor Software after correction of the center shift and beam hardening. To generate a complete image of the sample, four sectional images were normalized and stitched together, resulting in dimensions of 1025 × 1054 × 2751 voxels. A series of high-resolution, zoomed-in images with dimensions of 500 × 500 × 500 voxels were also obtained. To ensure consistent orientation throughout the experiment, all images were registered to the dry sample scans, with the Lanczos algorithm being employed for image resampling. Noise reduction and image smoothing were achieved using a non-local means filter, which preserved edge details.

Image segmentation was performed using a combination of differential imaging, interactive thresholding, and interactive top-hat filtering to distinguish the three phases: rock, brine, and CO_2. For each fractional flow, the brine phase was isolated by subtracting the dry image from the raw image, whereas the CO_2 phase was isolated by subtracting the raw image from the brine-saturated image. Large ganglia of the brine or CO_2 phases were identified through interactive thresholding, while small ganglia were captured using top-hat filtering. The segmented large and small ganglia were then merged to reconstruct the brine and CO_2 phases. Saturation was quantified from the segmented core scanning images, while other properties—including the distribution of the pore and throat radii, coordination number, interfacial curvature, contact angle, and shape factor (a measure of pore angularity)—were derived from the segmented high-resolution zoomed-in images, following the methods described by Raeini et al. [44], AlRatrout et al. [45], and Foroughi et al. [46].

2.2.2. SEM and EDS analysis

A Hitachi TM4000Plus SEM was employed to characterize the nanoscale mineral features before and after CO_2 injection. The SEM operated at an acceleration voltage of 15 kV, a beam current of 10 nA, and a temperature of 20 °C. Three adjacent samples, drilled from the same core, were used to observe the common mineral properties prior to CO_2 injection. The sample used in the steady-state imbibition relative permeability experiment was analyzed to assess the mineral characteristics following CO_2 injection. Initially, low-magnification imaging (×30) and EDS mapping were combined to obtain a cross-sectional view of the sample and identify the minerals types and their distribution [47]. High-magnification imaging was subsequently carried out field by field, combined with point EDS at the center of the minerals, to accurately characterize the diverse mineral features [48]. To ensure consistency and reliability, these mineral characteristics were consistently observed across multiple samples.

3. Results and discussion

3.1. Reactive flow characteristics

The measured relative permeabilities, along with the corresponding pressure differences and brine saturations, are presented in Fig. 2 [20,21,24,31,49–51]. As shown in Figs. 2(a) and (b), at the onset of imbibition (f_w = 0), the irreducible brine saturation is approximately 0.12, and the relative permeability of CO_2 reaches 0.47. This low initial brine saturation suggests a high capacity for CO_2 storage [49]. When the fractional flow is increased to f_w = 0.05, the brine saturation rises sharply to 0.51, while the CO_2 relative permeability decreases significantly to 0.013. This remarkable increase in brine saturation, coupled with the steep decline in CO_2 relative permeability, is likely due to brine—as the wetting phase—occupying a large fraction of the smaller pores and throats, trapping CO_2 and hindering its flow. As the brine saturation continues to increase, the relative permeability of the brine rises steadily, whereas the relative permeability of the CO_2 declines gradually. During this phase, the brine becomes more connected, facilitating its flow [49,52], while the flow of the CO_2 is progressively impeded, as demonstrated in Fig. 2(e).

The overall trend of our results is consistent with the special core analysis (SCAL) data from a larger sample (34 mm in diameter) from the same formation in a steady-state drainage experiment, confirming the reproducibility and accuracy of our results. Furthermore, when compared with other studies on sandstones without geochemical reactions [24,42,50,51], as illustrated in Fig. 2(a), a key distinguishing feature is the significantly lower CO_2 relative permeability observed under reactive conditions. For

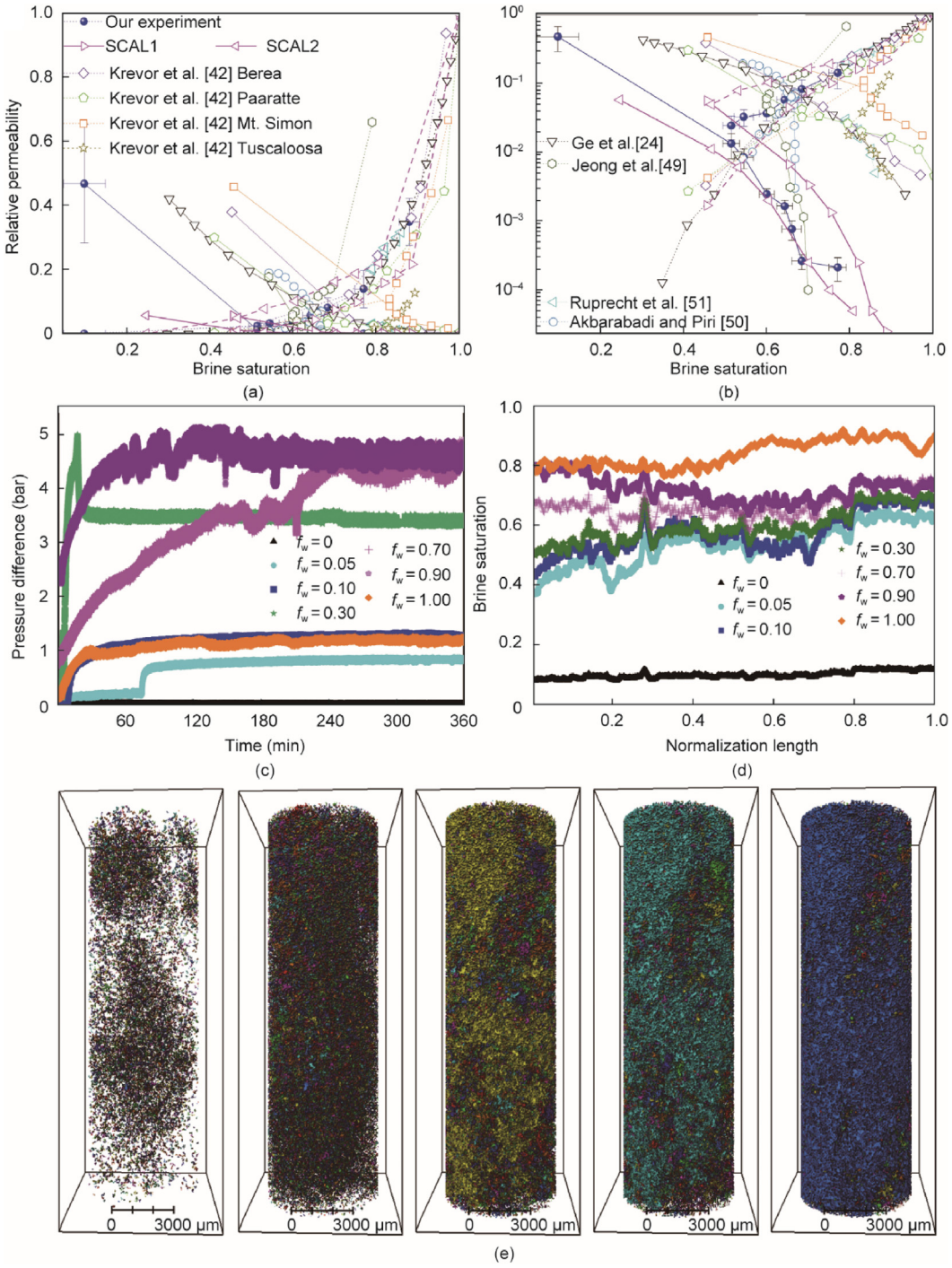

Fig. 2. Multiphase reactive flow in sandstone during CO_2 injection. (a, b) The experimental results are compared with SCAL data from drainage experiments conducted on a larger sample of the same formation, as well as with other published results. Imbibition experiments by Jeong et al. [49], Akbarabadi and Piri [50], and Ruprecht et al. [51] along with a drainage experiment by Ge et al. [24] all performed on Berea sandstone. Berea sandstone, primarily composed of quartz with minor amounts of feldspar and clay minerals [31], is known for its low chemical reactivity. Krevor et al. [42] provided drainage relative permeability measurements for Berea sandstone, as well as Paaratte, Mt. Simon, and Tuscaloosa sandstones. The relative permeability values in this study are referenced to the absolute permeability measured prior to CO_2 injection [20,21]. Error bars for brine saturation stem from segmentation uncertainties, while those for relative permeability result from uncertainties in pressure, viscosity, and injection rate, as noted in Appendix A. (c) Pressure difference and (d) brine saturation in f_w = 0, 0.05, 0.10, 0.30, 0.70, 0.90, and 1.00. (e) 3D rendering of the brine phase in f_w = 0, 0.1, 0.3, 0.7, and 0.9, with distinct colors to differentiate discrete clusters.

instance, in the Tuscaloosa sandstone examined by Krevor et al. [42], despite comparable petrophysical properties (absolute permeability: 220 vs 185 mD; porosity: 23.6% vs 25.0%), the relative permeability of CO_2 in reactive systems is reduced to approximately one-tenth of that in non-reactive cases. This observation correlates with the findings of Sun et al. [20] and Ge et al. [24], whose steady-state and unsteady-state relative permeability experiments on tight sandstone and Berea sandstone, respectively, revealed that reactive flow–rock interactions can increase brine flow capacity and enhance CO_2 trapping. However, the underlying

mechanisms may differ, as we observed a decrease in absolute permeability from (185 ± 10) to (110 ± 8) mD during CO_2 treatment, whereas those studies suggested an increase in permeability.

The reduction in CO_2 relative permeability, coupled with the decline in absolute permeability, is expected to impair CO_2 injectivity and diminish CO_2 storage capacity to a certain extent in both laboratory experiments and field-scale operations. A more comprehensive investigation into the petrophysical properties is essential to fully elucidate the mechanisms underlying this phenomenon, as detailed in the following section.

3.2. Analysis of changes in pore structure

Fig. 3 shows images of the sample and an analysis of the pore and throat structures before and after CO_2 injection, revealing significant variations. Fig. 3(a) highlights pore formation, enlargement, and shrinkage during CO_2 injection, as quantified in Fig. 3(b). The pore formation and enlargement, reflected in the increased porosity, are likely driven by mineral dissolution and the migration of fines [20,21,24]. In contrast, significant pore shrinkage, corresponding to a decrease in porosity, was also observed after CO_2 injection, likely due to secondary mineral precipitation and pore blockage by fines [25]. While these mineral reaction phenomena have been documented in previous studies using SEM [29–32], this study provides the first *in situ* pore-scale evidence. Although the average porosity increased, the enhanced heterogeneity impeded multiphase flow, as evidenced by the reduction in permeability.

Pore and throat size, coordination number, and shape factor provide quantitative insights into the alteration of the pore space during CO_2 injection. The coordination number, defined as the number of throats connected to a pore, decreases markedly after CO_2 injection (Fig. 3(d)), highlighting the reduction in pore connectivity. As shown in Fig. 3(e), CO_2 injection leads to a slight reduction in both pore and throat sizes, accompanied by a noticeable increase in the number of isolated elements. This indicates a significant reduction in flow pathways during CO_2 injection, consistent with the findings of Meng et al. [53], who investigated CO_2 storage in nanopores using molecular simulations and convincingly demonstrated, with robust evidence, that smaller pores are more effective for CO_2 trapping. Additionally, the shape factors of both pores and throats [44], as shown in Fig. 3(f), decrease, suggesting that the pores become more irregular in shape post-injection. This implies an increase in flow resistance. Consequently, the combined effects of reduced pore and throat sizes, diminished connectivity, and increased irregularity restrict the available flow pathways, leading to elevated flow resistance. This finding clarifies why, despite the increase in average porosity, the absolute permeability decreases.

Previous studies on changes in petrophysical properties have predominantly focused on porosity [14,17,18,21], with some providing pore size changes using nuclear magnetic resonance (NMR) [20,25]. However, looking at porosity alone is misleading because, even with significant dissolution, the pore becomes less well connected, resulting in decreases in the absolute and relative permeability.

Fig. 4 shows the measured distribution of the contact angle, the angle measured through the brine at which the two fluid phases meet the solid surface [45,54,55], and the curvature of the interfaces between the brine and CO_2. Two key trends emerge from Figs. 4(a) and (c). First, as the fractional flow of the brine (f_w) increases, the contact angle also increases, with the most frequent contact angle rising from 62.5° at f_w = 0.05 to 71.5° at f_w = 0.90. This suggests that the system is weakly water-wet, and that geochemical reactions in CO_2 injection reduce its water wettability. This observation aligns with the findings of Gholami and Raza [21], who measured brine droplet contact angles on sandstone before and after CO_2 treatment using the *ex situ* drop shape method under ambient conditions. Second, the range of contact angles broadens with increasing f_w, suggesting enhanced wettability heterogeneity, particularly in the less water-wet regions. These changes in wettability are expected to significantly facilitate brine flow and enhance CO_2 trapping, as reflected in the relative permeability measurements. Such alterations are likely driven by complex mineral reactions, which will be discussed in the following section.

As the fractional flow of brine (f_w) increases, the mean curvature of the CO_2–brine interface (Figs. 4(b) and (d)) gradually decreases, with the most frequent value declining from 0.046 μm^{-1} at f_w = 0.05 to 0.029 μm^{-1} at f_w = 0.90. This trend suggests that the interface becomes progressively flatter and smoother, which aligns with the observed reduction in water wettability. Using the Young–Laplace equation, this can be related to a reduction in capillary pressure from 3.2 kPa at f_w = 0.05 to 2.0 kPa at f_w = 0.9, which is as expected showing a decrease in capillary pressure, with saturation as displacement proceeds. Compared with that at a low f_w, CO_2 trapping at a higher f_w with lower capillary pressure is significantly reduced [25], facilitating easier flow and aligning with the contact angle and relative permeability results.

This paper presents, for the first time, *in situ* pore-scale characteristics of interface properties, including contact angle and curvature. These findings bridge geophysical property alterations and changes in relative permeability, providing direct pore-scale evidence of the mechanisms driving multiphase flow in subsurface environments.

3.3. Mineral reactions

The mineral compositions of the sandstones, as revealed by SEM and EDS mapping in Fig. 5, illustrate the mineralogical changes induced by CO_2 injection. Prior to CO_2 exposure, the sandstone is composed of elements including O, Si, C, Fe, Al, Ca, K, Na, and S, as shown in Fig. 5(a). Based on elemental distributions and previous studies [47], the dominant minerals are inferred to include quartz, feldspar, albite, kaolinite, calcite, gypsum, and siderite. The presence of carbon is likely due to residual organic matter from the depleted gas reservoir [56]. Quartz and feldspar form the primary framework minerals, while albite, kaolinite, calcite, and gypsum occur in smaller, more scattered concentrations as cementing phases.

Post-CO_2 injection, Fig. 5(b) reveals that only O, Si, C, Al, K, and Fe are detected, indicating the presence of quartz, feldspar, kaolinite, and siderite. Notably, Na, Ca, and S—associated with albite, calcite, and gypsum—are absent, suggesting that these minerals have undergone significant reactions and interactions during CO_2 injection. These are the underlying mechanisms driving the aforementioned alterations in petrophysical and interfacial properties, as well as relative permeability [33,48]. The dissolution of calcite during CO_2 injection has been widely reported [18,21,25]. The reactions and interactions of albite, gypsum, and other minerals during CO_2 injection will be explored in detail in the following high-resolution images.

As illustrated in Fig. 6, different minerals exhibit distinct reactions to CO_2 injection. Before CO_2 exposure, quartz presents a smooth, intact surface (Fig. 6(a)); following exposure, however, minor etch pits appear (Fig. 6(b)). Feldspar, which shows some surface alteration prior to CO_2 contact while retaining its structural integrity (Fig. 6(c)) [5,51], undergoes more pronounced changes post-injection, including the formation of laminar channels, etch pits, and crystal fragmentation (Fig. 6(d)). These alterations, coupled with the potential migration of feldspar fragments, likely have a significant impact on pore structure and permeability.

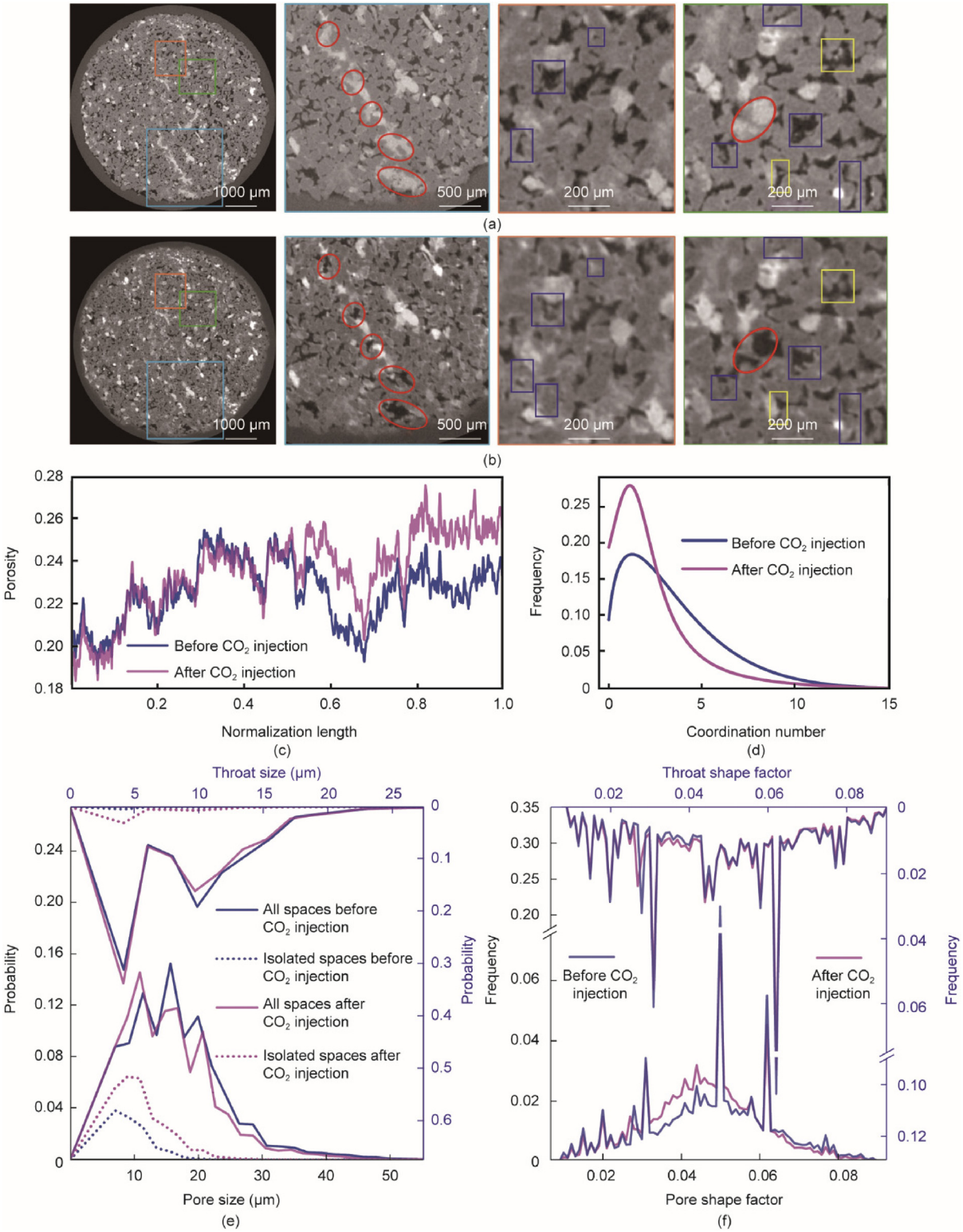

Fig. 3. Comparison of the pore structure before and after CO_2 injection. (a, b) 2D cross-section of 3D dry images (a) before and (b) after CO_2 injection, highlighting mineral dissolution (red), secondary mineral precipitation (blue), and fines migration (yellow). (c) Porosity, (d) coordination number, (e) radius distribution, and (f) shape factors of pores and throats before and after CO_2 injection. The shape factor is defined as $G = \frac{A}{P^2}$, where A is the area and P is the perimeter.

Kaolinite, the primary cementing material, forms a booklet-like structure and extensively fills pores before CO_2 exposure (Fig. 6(e)). After CO_2 treatment, kaolinite migrates and accumulates, blocking small pores and throats, which increases reservoir heterogeneity and consequently hinders multiphase flow (Fig. 6(f)), as also observed by Othman et al. [13] and De Silva et al. [14] using SEM on post-CO_2 treated sandstone. Moreover, we observed newly formed, small kaolinite crystals "growing" on

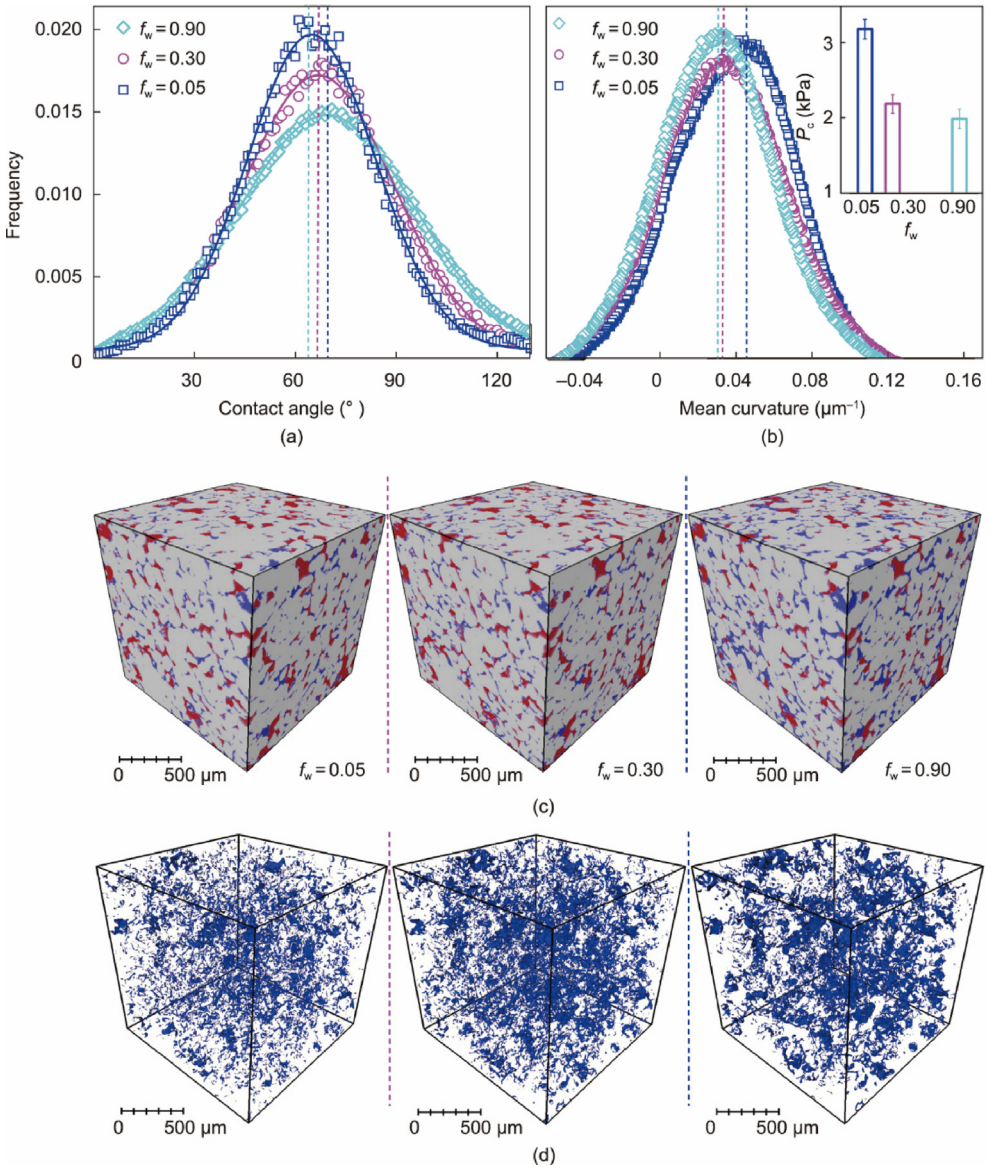

Fig. 4. *In situ* interfacial properties. (a) Contact angle, (b) mean curvature, and (inset) the calculated capillary pressure of the CO_2–brine–sandstone system at fractional flows, f_w, of 0.05, 0.30, and 0.90, along with the corresponding (c) CO_2–brine–sandstone distributions and (d) CO_2–brine interface for the same fractional flows. Capillary pressure is calculated using the Young–Laplace law: $P_c = 2\sigma k$, where σ is the interfacial tension and k is the mean curvature.

feldspar, as shown in Figs. 6(j) and (k). This is likely a result of feldspar and albite reacting with CO_2, leading to their transformation into kaolinite, which contributes to pore blockage and reduced permeability. This reaction plays a critical role in CO_2 storage, in line with the findings of Wang et al. [57], who were the first to quantify the contributions of mineral precipitation over the entire life cycle of a low-permeability tight sandstone reservoir by innovatively integrating experiments, transient well testing, and numerical simulations. Albite, which initially displays minor alterations as platy crystals with cleavage planes (Fig. 6(g)), disappears after CO_2 exposure, likely due to its transformation into feldspar through interaction with excess K^+ ions in the experimental brine.

Calcite, which is characterized by its rhombohedral cleavage, acts as a cement binding mineral grains (Fig. 6(h)). Its dissolution during CO_2 contact is well-documented and may promote fines migration, as suggested by Tang et al. [12]. Gypsum, which serves a role similar to that of calcite, exhibits some fragmentation even before CO_2 exposure (Fig. 6(i)), and its disappearance after treatment is likely due to fragmentation and migration caused by prolonged flushing.

4. Conclusions

Multiphase reactive flow plays a critical role in CO_2 injection into multi-mineral sandstones, directly affecting injectivity, storage capacity, and the long-term safety of CO_2 sequestration. To elucidate its mechanisms and impact, we performed steady-state imbibition relative permeability experiments, integrated with *in situ* X-ray imaging and *ex situ* SEM–EDS scanning on a sandstone with complex mineralogy from the putative storage site. The primary findings were as follows.

(1) A pronounced decline was observed in both CO_2 relative permeability and absolute permeability during multiphase reactive flow.

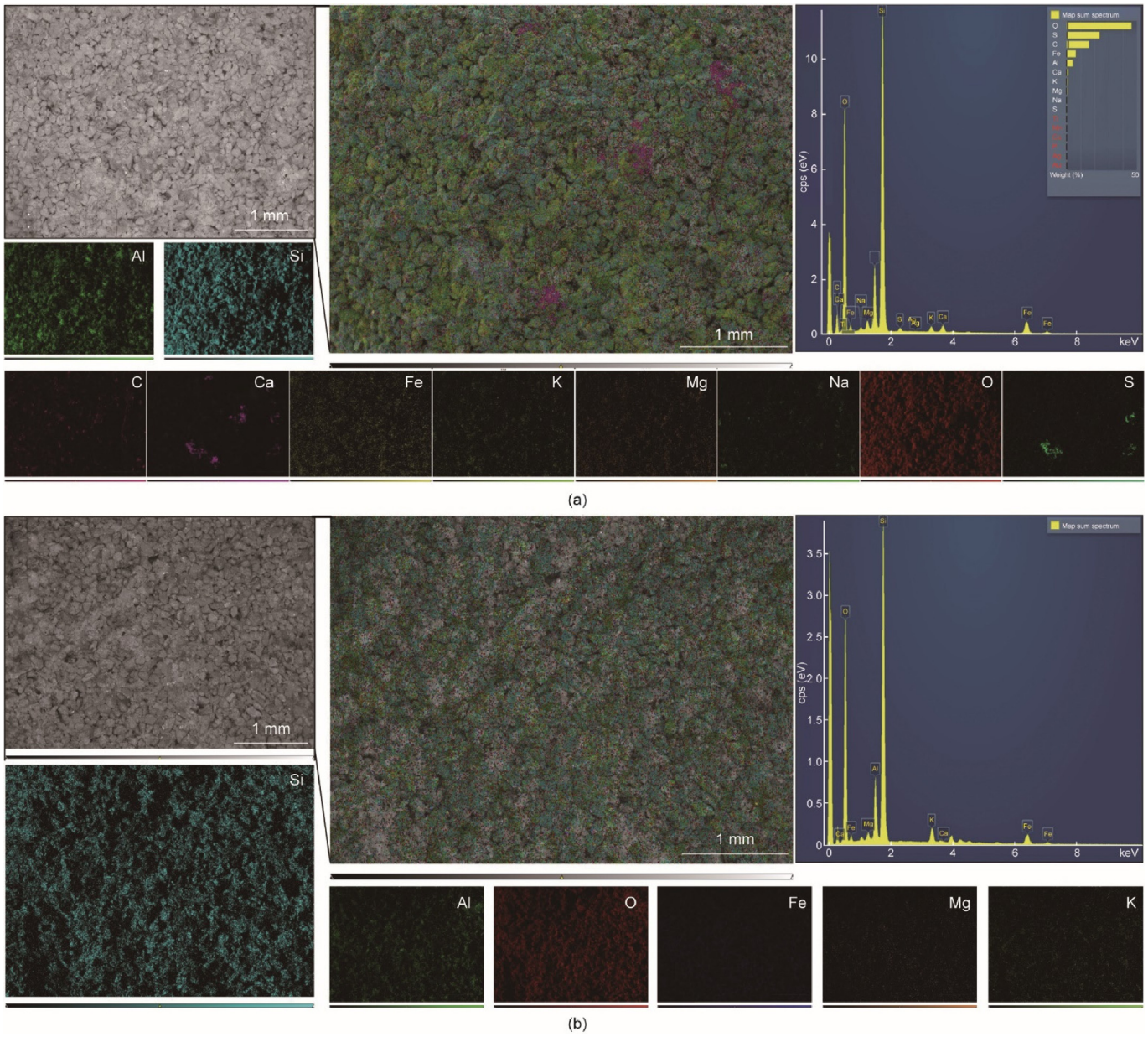

Fig. 5. Mineral compositions of sandstones from low-magnification SEM images and EDS mapping analysis. SEM images and EDS maps were obtained (a) before and (b) after CO_2 injection. The low-magnification SEM images provide an overview of the mineral characteristics, while the corresponding EDS maps show the exact elemental distributions. By combining these two techniques, the mineral composition and spatial distribution within the sample can be determined.

(2) Changes in petrophysical properties were identified, including reduced pore and throat sizes, diminished connectivity, and increased pore irregularity.

(3) The primary mechanisms included mineral dissolution, precipitation resulting from feldspar-to-kaolinite transformation, and fines migration.

Our study provides the first comprehensive analysis of multiphase reactive flow, establishing a foundation for improving injectivity, optimizing storage capacity, and ensuring long-term safety, particularly in mineralogically complex sandstone formations. For field-scale operations, it is essential to thoroughly characterize the mineralogical composition. In the case of complex sandstone formations, customized strategies—such as ion-mediated brine injection—should be employed to mitigate adverse reactions, as discussed earlier. Future research should focus on developing quantitative models to elucidate the relationships between permeability, petrophysical properties, and geochemical reactions, thereby improving predictions of CO_2 storage efficiency and safety in heterogeneous reservoirs.

CRediT authorship contribution statement

Rukuan Chai: Writing – original draft, Visualization, Methodology, Investigation, Formal analysis, Data curation, Conceptualization. **Qianqian Ma:** Writing – original draft, Methodology, Investigation, Formal analysis, Data curation. **Sepideh Goodarzi:** Methodology, Investigation, Formal analysis. **Foo Yoong Yow:** Writing – review & editing, Resources, Methodology. **Branko Bijeljic:** Writing – review & editing, Validation, Supervision, Methodology, Conceptualization. **Martin J. Blunt:** Writing – review & editing, Validation, Supervision, Resources, Project administration, Methodology, Conceptualization.

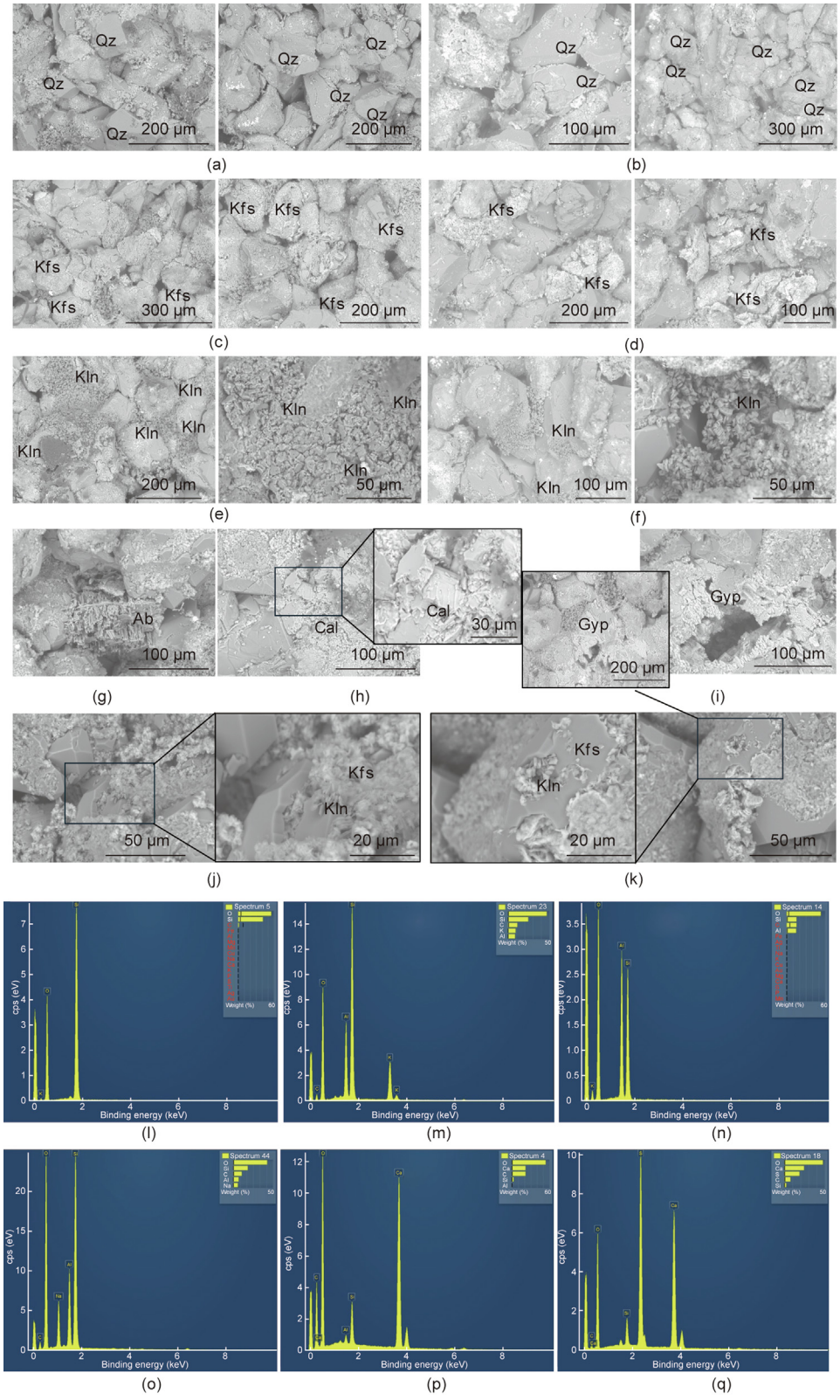

Fig. 6. Mineral characteristics from high-magnification SEM images and point-EDS data. (a, b) SEM images of quartz (Qz), (c, d) SEM images of feldspar (Kfs), and (e, f) SEM images of kaolinite (Kln), captured before and after CO_2 injection. (g–q) SEM images of (g) albite (Ab) and (o) its point-EDS data, (h) calcite (Cal) SEM image and (p) point-EDS data, and (i) gypsum (Gyp) SEM image and (q) point-EDS data, obtained prior to CO_2 injection. (j, k) Secondary mineral precipitation, specifically kaolinite, formed during CO_2 injection. (l–n) Point-EDS data for quartz, feldspar, and kaolinite, respectively.

Declaration of competing interest

The authors declare that they have no known competing financial interests or personal relationships that could have appeared to influence the work reported in this paper.

Acknowledgments

The authors gratefully acknowledge PETRONAS for their financial support and permission to publish this paper. We also extend our sincere gratitude to Anfal Al Zarafi, Aninditya Patmonoaji, Shanlin Ye, Edward Bailey, and Vincenzo Cunsolo for their invaluable assistance in conducting the experiments and analyzing the results.

Appendix A. Supplementary data

Supplementary data to this article can be found online at https://doi.org/10.1016/j.eng.2025.01.016.

References

[1] Luderer G, Vrontisi Z, Bertram C, Edelenbosch OY, Pietzcker RC, Rogelj J, et al. Residual fossil CO_2 emissions in 1.5–2 °C pathways. Nat Clim Chang 2018;8(7):626–33.
[2] Climate change 2021: the physical science basis. Contribution of working group I to the Sixth Assessment Report of the IPCC. Report. Cambridge: Cambridge University Press; 2021.
[3] Griscom BW, Adams J, Ellis PW, Houghton RA, Lomax G, Miteva DA, et al. Natural climate solutions. Proc Natl Acad Sci USA 2017;114(44):11645–50.
[4] Liu Y, Hu T, Rui Z, Zhang Z, Du K, Yang T, et al. An integrated framework for geothermal energy storage with CO_2 sequestration and utilization. Engineering 2023;30:121–30.
[5] He Y, Liu Y, Li J, Fan P, Liu X, Chai R, et al. Experimental study on the effect of CO_2 dynamic sequestration on sandstone pore structure and physical properties. Fuel 2024;375:132622.
[6] Cui G, Ren S, Rui Z, Ezekiel J, Zhang L, Wang H. The influence of complicated fluid–rock interactions on the geothermal exploitation in the CO_2 plume geothermal system. Appl Energy 2018;227:49–63.
[7] Luhmann AJ, Kong XZ, Tutolo BM, Ding K, Saar MO, Seyfried WE Jr. Permeability reduction produced by grain reorganization and accumulation of exsolved CO_2 during geologic carbon sequestration: a new CO_2 trapping mechanism. Environ Sci Technol 2013;47(1):242–51.
[8] Ma J, Querci L, Hattendorf B, Saar MO, Kong XZ. Toward a spatiotemporal understanding of dolomite dissolution in sandstone by CO_2-enriched brine circulation. Environ Sci Technol 2019;53(21):12458–66.
[9] Blunt MJ. Multiphase flow in permeable media: a pore-scale perspective. Report. Cambridge: Cambridge University Press; 2017.
[10] Shiraki R, Dunn TL. Experimental study on water–rock interactions during CO_2 flooding in the Tensleep Formation, Wyoming, USA. Appl Geochem 2000;15(3):265–79.
[11] Wang W, Yan Z, Chen D, He Y, Liang Z, Li Y, et al. The mechanism of mineral dissolution and its impact on pore evolution of CO_2 flooding in tight sandstone: a case study from the Chang 7 member of the Triassic Yanchang Formation in the Ordos Basin, China. Geoenergy Sci Eng 2024;235:212715.
[12] Tang Y, Lv C, Wang R, Cui M. Mineral dissolution and mobilization during CO_2 injection into the water-flooded layer of the Pucheng Oilfield, China. J Nat Gas Sci Eng 2016;33:1364–73.
[13] Othman F, Yu M, Kamali F, Hussain F. Fines migration during supercritical CO_2 injection in sandstone. J Nat Gas Sci Eng 2018;56:344–57.
[14] De Silva GD, Ranjith P, Perera M, Dai Z, Yang S. An experimental evaluation of unique CO_2 flow behaviour in loosely held fine particles rich sandstone under deep reservoir conditions and influencing factors. Energy 2017;119:121–37.
[15] Ochi J, Vernoux JF. Permeability decrease in sandstone reservoirs by fluid injection: hydrodynamic and chemical effects. J Hydrol 1998;208(3–4):237–48.
[16] Dávila G, Dalton L, Crandall DM, Garing C, Werth CJ, Druhan JL. Reactive alteration of a Mt. Simon Sandstone due to CO_2–rich brine displacement. Geochim Cosmochim Acta 2020;271:227–47.
[17] Lamy-Chappuis B, Angus D, Fisher Q, Grattoni C, Yardley BWD. Rapid porosity and permeability changes of calcareous sandstone due to CO_2–enriched brine injection. Geophys Res Lett 2014;41(2):399–406.
[18] Zou Y, Li S, Ma X, Zhang S, Li N, Chen M. Effects of CO_2–brine–rock interaction on porosity/permeability and mechanical properties during supercritical-CO_2 fracturing in shale reservoirs. J Nat Gas Sci Eng 2018;49:157–68.
[19] Tang Y, Hu S, He Y, Wang Y, Wan X, Cui S, et al. Experiment on CO_2–brine–rock interaction during CO_2 injection and storage in gas reservoirs with aquifer. Chem Eng J 2021;413:127567.
[20] Sun Y, Dai C, Yu Z, Xin Y. The carbonic acid–rock reaction in feldspar/dolomite-rich tightsand and its impact on CO_2–water relative permeability during geological carbon storage. Chem Geol 2021;584:120527.
[21] Gholami R, Raza A. CO_2 sequestration in sandstone reservoirs: how does reactive flow alter trapping mechanisms? Fuel 2022;324:124781.
[22] Sayegh SG, Krause FF, Girard M, DeBree C. Rock/fluid interactions of carbonated brines in a sandstone reservoir: Pembina Cardium, Alberta, Canada. SPE Form Eval 1990;5(4):399–405.
[23] Al-Yaseri A, Zhang Y, Ghasemiziarani M, Sarmadivaleh M, Lebedev M, Roshan H, et al. Permeability evolution in sandstone due to CO_2 injection. Energy Fuels 2017;31(11):12390–8.
[24] Ge J, Zhang X, Othman F, Wang Y, Roshan H, Le-Hussain F. Effect of fines migration and mineral reactions on CO_2–water drainage relative permeability. Int J Greenh Gas Control 2020;103:103184.
[25] Kou Z, Wang H, Alvarado V, Nye C, Bagdonas DA, McLaughlin JF, et al. Effects of carbonic acid–rock interactions on CO_2/brine multiphase flow properties in the upper minnelusa sandstones. SPE J 2023;28(02):754–67.
[26] Liu L, Suto Y, Bignall G, Yamasaki N, Hashida T. CO_2 injection to granite and sandstone in experimental rock/hot water systems. Energy Convers Manage 2003;44(9):1399–410.
[27] Kaszuba JP, Janecky DR, Snow MG. Carbon dioxide reaction processes in a model brine aquifer at 200 °C and 200 bars: implications for geologic sequestration of carbon. Appl Geochem 2003;18(7):1065–80.
[28] Ilgen AG, Aman M, Espinoza DN, Rodriguez MA, Griego J, Dewers TA, et al. Shale–brine–CO_2 interactions and the long-term stability of carbonate-rich shale caprock. Int J Greenh Gas Control 2018;78:244–53.
[29] Fu Q, Lu P, Konishi H, Dilmore R, Xu H, Seyfried W Jr, et al. Coupled alkali-feldspar dissolution and secondary mineral precipitation in batch systems. 1. New experiments at 200 °C and 300 bars. Chem Geol 2009;258(3–4):125–35.
[30] Lu P, Fu Q, Seyfried WE Jr, Hedges SW, Soong Y, Jones K, et al. Coupled alkali feldspar dissolution and secondary mineral precipitation in batch systems 2. New experiments with supercritical CO_2 and implications for carbon sequestration. Appl Geochem 2013;30:75–90.
[31] Dawson G, Pearce J, Biddle D, Golding S. Experimental mineral dissolution in Berea Sandstone reacted with CO_2 or SO_2–CO_2 in NaCl brine under CO_2 sequestration conditions. Chem Geol 2015;399:87–97.
[32] Pearce J, Dawson G, Blach TP, Bahadur J, Melnichenko YB, Golding SD. Impure CO_2 reaction of feldspar, clay, and organic matter rich caprocks: decreases in the fraction of accessible mesopores measured by SANS. Int J Coal Geol 2018;185:79–90.
[33] Pearce J, Dawson G, Golab A, Knuefing L, Sommacal S, Rudolph V, et al. A combined geochemical and μCT study on the CO_2 reactivity of Surat Basin reservoir and cap-rock cores: porosity changes, mineral dissolution and fines migration. Int J Greenh Gas Control 2019;80:10–24.
[34] Carroll SA, McNab WW, Dai Z, Torres SC. Reactivity of Mount Simon sandstone and the Eau Claire shale under CO_2 storage conditions. Environ Sci Technol 2013;47(1):252–61.
[35] Fuchs SJ, Espinoza DN, Lopano CL, Akono AT, Werth CJ. Geochemical and geomechanical alteration of siliciclastic reservoir rock by supercritical CO_2–saturated brine formed during geological carbon sequestration. Int J Greenh Gas Control 2019;88:251–60.
[36] Lin Q, Bijeljic B, Raeini AQ, Rieke H, Blunt MJ. Drainage capillary pressure distribution and fluid displacement in a heterogeneous laminated sandstone. Geophys Res Lett 2021;48:e2021GL093604.
[37] Fenghour A, Wakeham WA, Vesovic V. The viscosity of carbon dioxide. J Phys Chem Ref Data 1998;27(1):31–44.
[38] Lengyel S, Tamas J, Giber J, Holderith J. Study of viscosity of aqueous alkali halide solutions. J Acta Chim Acad Sci Hung 1964;40:125–43.
[39] Chalbaud C, Robin M, Lombard JM, Martin F, Egermann P, Bertin H. Interfacial tension measurements and wettability evaluation for geological CO_2 storage. Adv Water Resour 2009;32(1):98–109.
[40] Gao Y, Raeini AQ, Selem AM, Bondino I, Blunt MJ, Bijeljic B. Pore-scale imaging with measurement of relative permeability and capillary pressure on the same reservoir sandstone sample under water-wet and mixed-wet conditions. Adv Water Resour 2020;146:103786.
[41] Alhammadi AM, Gao Y, Akai T, Blunt MJ, Bijeljic B. Pore-scale X-ray imaging with measurement of relative permeability, capillary pressure and oil recovery in a mixed-wet micro-porous carbonate reservoir rock. Fuel 2020;268:117018.
[42] Krevor SCM, Pini R, Zuo L, Benson SM. Relative permeability and trapping of CO_2 and water in sandstone rocks at reservoir conditions. Water Resour Res 2012;48(2):W02532.
[43] Gao Y, Lin Q, Bijeljic B, Blunt MJ. Pore-scale dynamics and the multiphase Darcy law. Phys Rev Fluids 2020;5(1):013801.
[44] Raeini AQ, Bijeljic B, Blunt MJ. Generalized network modeling: network extraction as a coarse-scale discretization of the void space of porous media. Phys Rev E 2017;96(1):013312.
[45] AlRatrout A, Blunt MJ, Bijeljic B. Wettability in complex porous materials, the mixed-wet state, and its relationship to surface roughness. Proc Natl Acad Sci USA 2018;115(36):8901–6.
[46] Foroughi S, Bijeljic B, Lin Q, Raeini AQ, Blunt MJ. Pore-by-pore modeling, analysis, and prediction of two-phase flow in mixed-wet rocks. Phys Rev E 2020;102(2):023302.
[47] Pettijohn FJ, Potter PE, Siever R. Sand and sandstone. Berlin: Springer Science & Business Media; 2012.

[48] Chai R, Liu Y, Xue L, Rui Z, Zhao R, Wang J. Formation damage of sandstone geothermal reservoirs: during decreased salinity water injection. Appl Energy 2022;322:119465.
[49] Jeong GS, Lee J, Ki S, Huh DG, Park CH. Effects of viscosity ratio, interfacial tension and flow rate on hysteric relative permeability of CO_2/brine systems. Energy 2017;133:62–9.
[50] Akbarabadi M, Piri M. Relative permeability hysteresis and capillary trapping characteristics of supercritical CO_2/brine systems: an experimental study at reservoir conditions. Adv Water Resour 2013;52:190–206.
[51] Ruprecht C, Pini R, Falta R, Benson S, Murdoch L. Hysteretic trapping and relative permeability of CO_2 in sandstone at reservoir conditions. Int J Greenh Gas Control 2014;27:15–27.
[52] Abdoulghafour H, Sarmadivaleh M, Hauge LP, Fernø M, Iglauer S. Capillary pressure characteristics of CO_2–brine–sandstone systems. Int J Greenh Gas Control 2020;94:102876.
[53] Meng S, Liu C, Liu Y, Rui Z, Liu H, Jin X, et al. CO_2 utilization and sequestration in organic-rich shale from the nanoscale perspective. Appl Energy 2024;361:122907.
[54] Alhosani A, Lin Q, Scanziani A, Andrews E, Zhang K, Bijeljic B, et al. Pore-scale characterization of carbon dioxide storage at immiscible and near-miscible conditions in altered-wettability reservoir rocks. Int J Greenh Gas Control 2021;105:103232.
[55] Blunt MJ, Lin Q, Akai T, Bijeljic B. A thermodynamically consistent characterization of wettability in porous media using high-resolution imaging. J Colloid Interface Sci 2019;552:59–65.
[56] Punase A, Prakoso A, Hascakir B. Effect of clay minerals on asphaltene deposition in reservoir rock: insights from experimental investigations. Fuel 2023;351:128835.
[57] Wang X, Yang H, Huang Y, Liang Q, Liu J, Ye D. Evolution of CO_2 storage mechanisms in low-permeability tight sandstone reservoirs. Engineering. In press.